Hybrid Hollow Microlattices With Unique Combination of Stiffness and Damping

L. Salari-Sharif
Mechanical and Aerospace Engineering Department, University of California, Irvine, Irvine, CA 92697
e-mail: lsalaris@uci.edu

T. A. Schaedler
Sensors and Materials Lab, HRL Laboratories, LLC, Malibu, CA 90265
e-mail: taschaedler@hrl.com

L. Valdevit[1]
Mechanical and Aerospace Engineering Department, University of California, Irvine, Irvine, CA 92697
e-mail: valdevit@uci.edu

Hybrid micro-architected materials with unique combinations of high stiffness, high damping, and low density are presented. We demonstrate a scalable manufacturing process to fabricate hollow microlattices with a sandwich wall architecture comprising an elastomeric core and metallic skins. In this configuration, the metallic skins provide stiffness and strength, whereas the elastomeric core provides constrained-layer damping. This damping mechanism is effective under any strain amplitude, and at any relative density, in stark contrast with the structural damping mechanism exhibited by ultralight metallic or ceramic architected materials, which requires large strain and densities lower than a fraction of a percent. We present an analytical model for stiffness and constrained-layer damping of hybrid hollow microlattices, and verify it with finite elements simulations and experimental measurements. Subsequently, this model is adopted in optimal design studies to identify hybrid microlattice geometries which provide ideal combinations of high stiffness and damping and low density. Finally, a previously derived analytical model for structural damping of ultralight metallic microlattices is extended to hybrid lattices and used to show that ultralight hybrid designs are more efficient than purely metallic ones. [DOI: 10.1115/1.4038672]

Keywords: sandwich structures, constrained-layer damping, buckling mechanism, energy dissipation, cellular materials

1 Introduction

Cellular materials provide a unique platform for multifunctional applications and have been widely investigated over the past two decades. Cellular materials are well known for their low densities, unique mechanical, electrical, thermal, acoustic, and bio-compatibility properties [1–5] and have been used in lightweight structures, impact protection [6–8], active cooling [9,10], sound absorption [11], and medical implants [12–14]. The effective properties of periodic cellular materials are uniquely determined by the physical properties of their constituent phase(s) and their topological arrangement in the unit cell. Careful design of the unit cell architecture, generally performed by geometric or topology optimization techniques, can result in architected materials with mechanical and functional properties vastly superior to those of stochastic materials (e.g., foams). Notable examples include architected materials optimized for specific stiffness and strength [15,16], active cooling performance [17], sound absorption [18], and impact protection [19].

Stochastic cellular materials have been used for vibration isolation and damping for a long time [1,20,21]. More recent studies have shown that the damping performance of cellular materials can be enhanced by careful design of the periodic unit cell architecture, e.g., by incorporating intrinsically dissipative elements (e.g., elastomers) [22] or negative stiffness subcomponents [23,24]. These complex architected materials designs, though, remain difficult to fabricate with scalable approaches.

Recent progress in additive manufacturing has enabled scalable fabrication of novel hollow microlattices with wall thicknesses as small as a few hundred nanometers, and overall dimensions at the tens of centimeters scale, resulting in dimensional control over seven orders of magnitude in length scale [25]. Sacrificial dense polymeric lattices are fabricated by a self-propagating polymer waveguide polymerization process [26,27], and subsequently coated with the structural material of choice, before polymer removal [25,28]. The mechanical properties of these single layer hollow lattices have been experimentally investigated [29–31], and models have been developed for their stiffness [32] and strength [33]. A unique feature of ultralight metallic hollow microlattices is their ability to fully recover their shape after experiencing compressive strains in excess of 50%. This is enabled by their very small wall thickness to bar diameter ratios, which allow local elastic buckling of the bars, and subsequent rotation about the pinched location without the accumulation of plastic strain [30]. During a loading-unloading cycle, a considerable fraction of the elastic energy is dissipated, resulting in very high damping capacity. The authors have extensively investigated this unique energy dissipation mechanism [29]. Through a combination of experiments and modeling efforts, the contributions to the damping capacity of the lattice from six different physical mechanisms were isolated and quantified, as a function of the strain amplitude under cyclic loading. Under small strain amplitudes (less than a few percent), the damping capacity (of the order of 0.25) is attributed to microfriction at sharp wall crack edges and intrinsic material damping (responsible for about 50% of the total damping capacity), fracture and plastic deformation of the walls (~30%), and viscous dissipation from the air inside and around the hollow bars (~20%). Conversely, under large strain amplitudes (of the order of 50%), the largest contribution comes from elastic local buckling of the bars and macroscopic friction emerging from bar-to-bar contact (a structural damping mechanism, accounting for ~60% of the total damping capacity), followed by fracture and plasticity (~19%), microfriction and intrinsic damping (~17%), and a small amount of viscous damping (4%). The conclusion is that the largest gain from an optimal design perspective is in maximizing the elastic buckling contribution for large strain

[1]Corresponding author.

Contributed by the Materials Division of ASME for publication in the Journal of Engineering Materials and Technology. Manuscript received June 25, 2017; final manuscript received October 11, 2017; published online February 14, 2018. Assoc. Editor: Curt Bronkhorst.

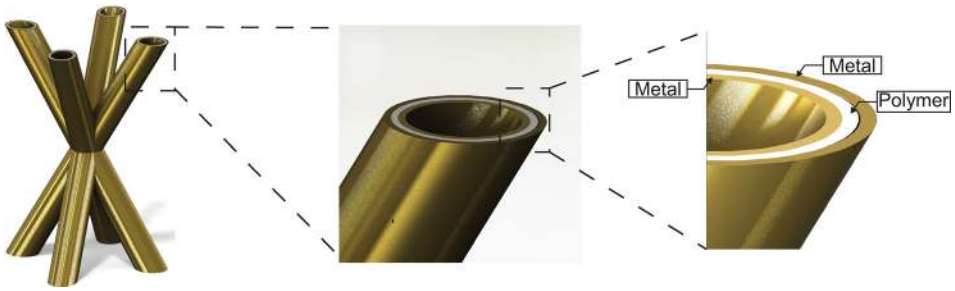

Fig. 1 Schematic of the unit cell of a hybrid (metal/polymer/metal) lattice

applications and maximizing the intrinsic damping for small strain applications.

Previous work focused on the former strategy [29]. A simple analytical tool was developed to capture this energy loss and verified experimentally. Finally, an optimal design tool was implemented based on the analytical model to identify the lattice geometries that maximize specific stiffness and damping efficiency, specifically for the material group $E^{1/3}\tan\delta/\rho$, with E the Young's modulus, ρ the mass density and $\tan\delta$ the damping coefficient of the material. One important conclusion is that these materials exhibit very high values of this figure of merit, but only when manufactured at very low relative density ($\bar{\rho} < 0.1\%$). As the density is increased beyond this level, the wall thickness becomes too high to enable large scale rotation of bars after local buckling without introducing any permanent plastic deformation. As the total amount of energy loss is as important from an application standpoint as the damping coefficient, the efficiency of these materials as stiff dampers is limited. In order to design higher density lattices with exceptional combinations of specific stiffness and damping, we propose to fabricate lattices with sandwich walls, whereby two metallic layers enclose a lossy polymeric film (Fig. 1). When the hybrid lattice is compressed, the lossy layer deforms (primarily in shear), dissipating energy. This approach is akin to classic constrained-layer damping, widely exploited in flat aircraft structure design [34,35]. Importantly, this mechanism has the potential to dramatically increase the intrinsic contribution to the damping capacity of microlattices, which, as discussed earlier, is the key mechanism under small strains. Moreover, the thickening of the wall resulting from the addition of the polymer results in higher buckling strength, and hence, higher values of structural damping, which as discussed before is the most influential mechanism under large strains. This intrinsic damping mechanism can emerge as the exclusive damping mechanism in lattices of high relative density or it can appear in tandem with the structural damping mechanism (albeit, exclusively in ultralight lattices, and only at relatively large strain amplitudes).

While wall hybridization has the potential to substantially increase intrinsic material damping and structural damping in microlattices, no detrimental effect is expected on the other damping mechanisms. While the toughness of the hybrid wall is expected to be higher than for the metallic wall, fewer through-cracks will be present, so the total amount of energy dissipated in fracturing of the walls during cycling loading—albeit likely impossible to predict analytically—is probably quite similar in metallic and hybrid lattices. Elastomeric substrates are known to stabilize the plastic deformation of metallic films, hence the plastic work contribution will likely increase. The smaller population of through-cracks in hybrid lattices could result in a potential decrease of microfriction, but this will be likely offset by an increase in viscous damping—due to the higher confinement of the air inside the hollow bars. Finally, macroscale friction, i.e., bar-to-bar friction during large deformations, is not expected to change, as the specific surface area of the lattice is nearly identical.

This work focuses on fabricating, characterizing, modeling, and optimizing hybrid hollow microlattices, with the overarching goal of designing lattices with unique combinations of high stiffness, high damping, and low density.

The paper is organized as follows: The manufacturing process is explained in detail in Sec. 2. Section 3 presents an analytical model for stiffness and constrained-layer damping mechanisms, followed by numerical validation and experimental verification. The structural damping mechanism is studied numerically in Sec.

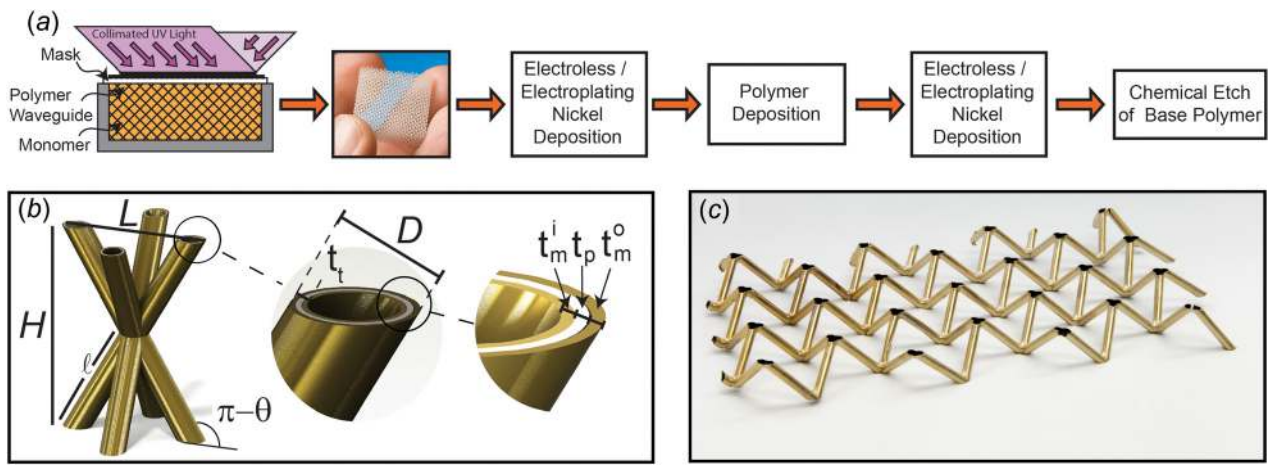

Fig. 2 (*a*) Schematic of the proposed fabrication process for hybrid hollow microlattice materials, (*b*) octahedral unit cell topology and defining dimensional parameters, and (*c*) a sample of a tetrahedral hybrid hollow microlattice

4 and a suitable analytical model is presented. Finally, the models presented in Secs. 3 and 4 are used for optimal design studies in Sec. 5. Conclusions are reported in Sec. 6.

2 Fabrication Process and Geometric Characterization

Hybrid hollow microlattice materials are fabricated with a multistep additive manufacturing process (Fig. 2(*a*)): (i) fabrication of a sacrificial polymeric template by a self-propagating photopolymer waveguide process [25,27,36]; (ii) coating of the template with a metallic film by a suitable deposition process (e.g., electroless and/or electroplating); (iii) coating of the resulting metal layer with a film of polymer by suitable deposition process; (iv) coating of the resulting polymeric layer with another metallic film; and (v) removal of the sacrificial polymeric template by chemical etching.

In the first step, the polymeric templates are fabricated by exposing a thiolene liquid photomonomer to collimated ultraviolet (UV) light impinging via a patterned mask from different directions. When the UV light reaches the thiolene liquid through the holes in the mask, waveguides are formed and a periodic array of tubes emerges; when multiple beams approaching from different directions intersect, nodes are formed. A wide range of architectures, such as tetrahedral [27] or octahedral [26], can be manufactured by changing the mask pattern and the incident angle of the UV light rays. The polymeric lattices are then used as a template for depositing the first (internal) metallic film. Although different metals can be deposited with suitable deposition techniques (e.g., nickel, copper, and gold) [28], all samples in this work used a combination of electroless and electrodeposited Nickel. The former is used to start the growth process on a nonconductive substrate and is limited to a thickness of a few micrometers (~3 min deposition time); electrodeposited nickel is then applied to reach the desired metallic film thickness. The polymeric layer is then deposited on top of the metallic lattice by dip coating in a solution of thermoplastic polyurethane (TPU) in tetrahydrofuran, followed by drying. Alternatively, very uniform coatings of poly (p-xylylene) polymers (Parylene®) can be deposited by chemical vapor deposition. A variety of polymers can be deposited on the metallic lattices; for this study, TPU is chosen. Subsequently, another metallic layer is deposited on top of the polymeric layer. Finally, the top and bottom edges of the samples are sanded to expose the underlying base polymer at each external node; the sacrificial polymeric template is etched out by using a base solution (3M NaOH at 60 deg) (the solution must be chosen in a way to remove only the base inner polymeric template and not the polymer in the constrained-layer), resulting in hybrid hollow tube microlattices.

This process was used to generate hollow lattices with the octahedral topology shown in Fig. 2(*b*), which is built of bars with length ℓ, diameter D, inner layer metal wall thickness t_m^i, polymer wall thickness t_p, outer layer metal wall thickness t_m^o, and truss angle θ.

Figure 2(*c*) shows a half-layer tetrahedral hybrid lattice. The truss angle, length, and diameter of the lattice bars are measured by a Dino digital microscope. This lattice contains bars with a length $\ell = 22.4$ mm, a diameter $D = 3.2$ mm, and a truss angle $\theta = 47$ deg (Fig. 3(*a*)). The wall thickness of the three different layers was measured by scanning electron microscopy of one bar. The bar was extracted from the lattice and fixed in epoxy resin. The resin was sanded with sand paper at varying roughness down to 1 μm in order to achieve a uniform cross section. Electroplating and electroless nickel plating result in conformal coatings with a uniform thickness that can be controlled by the plating time. As a result, the inner and outer nickel layers appear reasonably uniform, with an average thickness of $t_m^i = 19.5\,\mu$m and $t_m^o = 15.1\,\mu$m. By contrast, the dip coating process results in a very nonuniform TPU layer thickness, varying between $t_p = 1.5\,\mu$m and $t_p = 31\,\mu$m (Figs. 3(*b*) and 3(*c*)). As these measurements have been performed on a single bar in the lattice, we expect the distribution in polymer thickness across the entire sample to be even broader.

The mechanical properties of the TPU layers are measured by dynamic mechanical analysis at a frequency of 1 Hz. The TPU layer has a density, $\rho = 1200\,\text{kg/m}^3$, Young's modulus, $E = 1.4$ GPa, and a damping coefficient $\tan\delta = 0.25$. The properties of the nickel layer had been measured in the previous work: density $\rho = 8900\,\text{kg/m}^3$, Young's modulus $E = 165.8$ GPa, yield strength $\sigma_y = 607$ MPa, and negligible damping [30].

3 Stiffness and Constrained-Layer Damping Analysis

3.1 Analytical Modeling. A free body diagram of a bar within the microlattice subjected to uniaxial compression is depicted in Fig. 4. Under this loading condition, each bar experiences a combination of axial compression, transverse shear, and bending moment.

The stiffness of the unit cell can be extracted with the "principle of virtual work." The energy stored in each bar includes axial, shear, and bending contributions. Each of these energy terms can be readily expressed in analytical form by classic elastic beam theory. By imposing that the energy stored in the unit cell is equal to the external work $U = (1/2)P\delta$, with P being the external load on the cell and δ the cell displacement, the unit cell stiffness (defined as $k = P/\delta$) can be calculated and properly rescaled to obtain the effective Young's modulus of the lattice. To capture the viscoelastic nature of the polymeric layer, its elastic moduli are treated as complex numbers (viscoelastic correspondence principle). As the viscoelastic properties of the polymer (stiffness and damping) are generally a function of frequency, the properties of

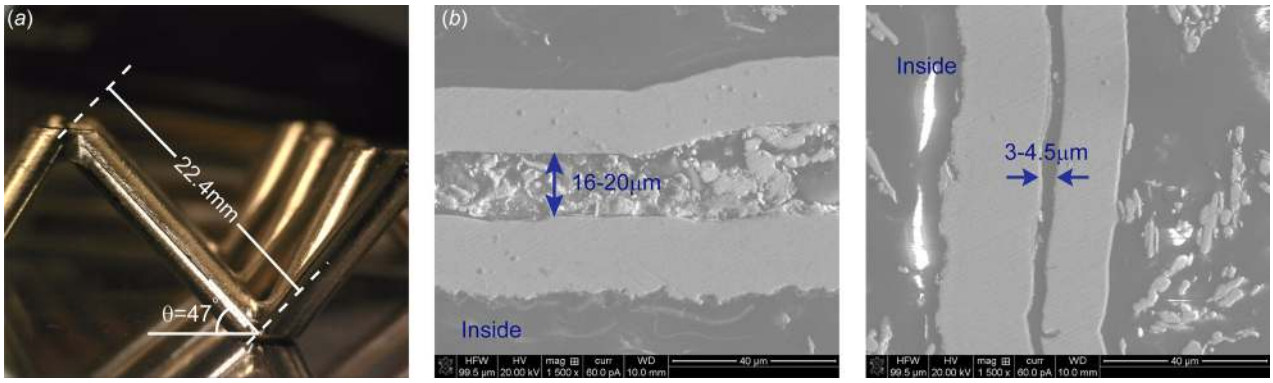

Fig. 3 (*a*) Length and angle measurements of hybrid hollow microlattices via a Dino digital microscope; (*b*) and (*c*) variations in polymer layer thickness of bar walls measured by scanning electron microscopy at two locations on a single cross section of the same bar

the hybrid lattice itself will be frequency dependent. The complex modulus of the lattice can be written as

$$E^*_{\text{lattice}}(\omega) = \frac{3\pi D^3 t_t E^*_{\text{voigt}}(\omega)\sin\theta}{\ell^4\cos^4\theta}\left(1+\frac{3}{2}\left(\frac{D}{\ell}\right)^2\tan^2\theta + 3\frac{E^*_{\text{voigt}}(\omega)}{G^*_p(\omega)}\frac{t_t}{t_p}\left(\frac{D}{\ell}\right)^2 \Big/ \left(1+\frac{t^i_m+t^o_m}{t_p}\frac{G_m}{G^*_p(\omega)}\right)\right)^{-1} \tag{1}$$

with all geometric parameters defined in Fig. 2(*b*). Note that in the analytical model, the thickness of inner metal layer, outer metal layer, and polymeric layer is assumed to be uniform throughout the sample. Both the polymer and the metal are assumed isotropic, whereby the shear modulus is related to Young's modulus by $G = (E/2(1+\nu))$. For the polymer, we assume Poisson's ratio $\nu_p = 0.5$ (incompressibility limit), resulting in $G^*_p = (E^*_p/3)$; for the metal, we assume $\nu_m = 0.3$. Note that Poisson's ratio is assumed to be frequency independent. Finally, E^*_{voigt} represents the effective longitudinal Young's modulus of the hybrid wall, i.e.,

$$E^*_{\text{voigt}} = E_m\frac{t^i_m+t^o_m}{t_t} + E^*_p\frac{t_p}{t_t} \tag{2}$$

where E^*_p and E_m are Young's modulus of the polymer (a complex number) and metal, respectively.

As the effective Young's modulus of the lattice is a complex number ($E^*_{\text{unit\_cell}} = E'_{\text{unit\_cell}} + iE''_{\text{unit\_cell}}$), the intrinsic damping coefficient can be extracted from the storage modulus ($E'_{\text{unit\_cell}}$) and the loss modulus ($E''_{\text{unit\_cell}}$) as

$$\tan\delta = \frac{\text{Im}(E^*_{\text{unit\_cell}})}{\text{Re}(E^*_{\text{unit\_cell}})} = \frac{E''_{\text{unit\_cell}}}{E'_{\text{unit\_cell}}} \tag{3}$$

The density of the lattice, obtained by simple geometric considerations, can be expressed as

$$\rho = \frac{2\pi}{\sin\theta\cos^2\theta}\frac{D}{\ell}\left(\rho_m\frac{t^i_m+t^o_m}{\ell}+\rho_p\frac{t_p}{\ell}\right) \tag{4}$$

where ρ_m is the density of metal and ρ_p is the density of the polymer. Note that any mass accumulation at the nodes is neglected.

3.2 Model Validation by Finite Elements Analysis. Finite elements (FE) analyses are performed using the commercial finite element package ABAQUS to validate the accuracy of the analytical model. The nickel layer (metal skins) is modeled as a linear elastic material, and the TPU layer (polymeric core) is modeled as a viscoelastic material. The material properties provided in Sec. 2 are used for all simulations. The steady-state-dynamics-direct algorithm at frequency of 1 Hz is used to capture the viscoelastic behavior of the materials. Preliminary calculations confirmed that this algorithm provides reliable estimates of the viscoelastic properties of simple composite materials (Voigt and Reuss configurations).

Simulations are performed on two different configurations: (i) individual hollow bars (Fig. 5(*a*)) and (ii) single unit cells (Fig. 5(*b*)). The individual bars are loaded with an inclined force to capture the combination of axial and shear load. To ensure that a moment develops consistent with the free body diagram in Fig. 4, the bottom edge is fixed, while the top edge is allowed to move in all directions (albeit as a rigid body) but not allowed to rotate (Fig. 5(*a*). The unit cell is loaded uniaxially in compression and prevented from rotating at the sides. To represent an infinite lattice that deforms uniformly (i.e., each unit cell has exactly the same deformed shape), the following boundary conditions are applied: the nodes on the –*z* face are constrained from moving in *z*

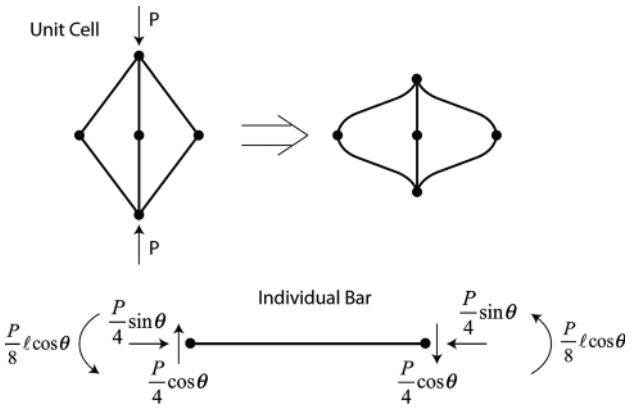

Fig. 4 Schematic of the deformation of a lattice unit cell under uniaxial external compression, combined with the free-body diagram of a single bar in the unit cell. The bar undergoes a combination of transverse shear load, axial load, and bending moment.

but allowed to move along *x* and *y*; the nodes on the +*z* face are subjected to a downward displacement δ; the nodes on the $\pm x$ faces are all required to move by the same unspecified amount in the *x* direction, and let free to move along *y* and *z*; the nodes on the $\pm y$ faces are all required to move by the same unspecified amount in the y direction, and let free to move along *x* and *z*; finally, all rotations are prevented at all nodes on the $\pm x$, $\pm y$, and $\pm z$ faces. These conditions are imposed by constraining all the nodes on each face with reference points along specific degrees-of-freedom and applying boundary conditions to the reference points (Fig. 5(*b*)).

Configuration (ii) includes a node at the center, and hence, a comparison of (i) and (ii) allows quantification of nodal effects. For each configurations, two samples are modeled: a slender sample, with an aspect ratio, $\ell/D = 8$, $t_t/D = 0.007$ (Sample A) and a stubby sample, with an aspect ratio, $\ell/D = 4$, $t_t/D = 0.1$ (Sample B). All dimensions are provided in Table 1. Sample A is modeled with shell elements (with the three wall layers homogenized via classic lamination theory), whereas sample B is modeled with solid elements, with full meshing of the three wall layers. The solid bar and unit cell contain 18 elements across the thickness and sufficient number of elements (mostly with aspect ratio of one) along the length.

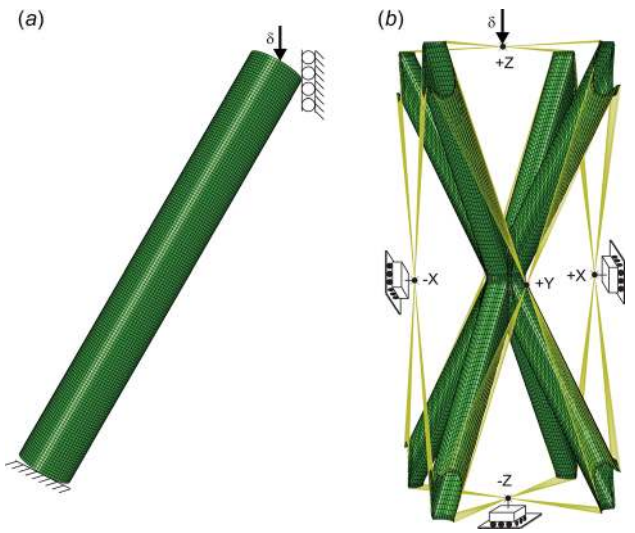

Fig. 5 Load and boundary conditions on (*a*) single bar and (*b*) single unit cell

Table 1 Summary of geometrical properties of the samples and Young's modulus and damping coefficient captured from analytical model of single bar, and FE simulation of single bar and single unit cell for each sample

						FE simulation of single bar		FE simulation of unit cell		Analytical model	
Sample	Strut length (μm)	Strut diameter (μm)	Wall thickness of TPU (μm)	Wall thickness of nickel (μm)	Strut angle (deg)	E (MPa)	tanδ ($\times 10^{-4}$)	E (MPa)	tanδ ($\times 10^{-4}$)	E (MPa)	tanδ ($\times 10^{-4}$)
A	4000	500	2.5	0.5	60	11.4	8.60	5.17	6.71	11.56	8.55
B	1000	250	16.6	4.16	60	2580	8.53	2740	28.0	2060	6.70

The complex Young's modulus of the lattice is extracted from the simulations (by using the real and the imaginary part of force in $E = (FL/A\delta)$) and compared with the analytical prediction from Eq. (1) and the results are presented in Table 1. Note that the simulations are performed under a small strain of 1% to eliminate the effects of large deformation and to accurately capture intrinsic damping.

For sample A ($\ell/D = 8$), the results indicate that the analytical model can capture the behavior of a single bar accurately; however, it overestimates the unit cell stiffness. The same discrepancy was also observed in single layer metallic lattices with the same aspect ratios in previous studies [32]. We attribute this discrepancy to the fact that simple beam model does not capture the effects of the nodes.

For sample B ($\ell/D = 4$), the storage modulus captured by the FE simulation for the single bar and single unit cell is very close; however, the analytical model is underpredicting the modulus in both simulations by ~20%. We attribute this discrepancy to the sample geometry: the wall thickness in sample B ($t_t/D = 0.1$) violates the thin-wall assumption in the analytical model. On the other hand, the damping of the lattice captured by the FE simulation on the unit cell mesh is ~4× higher than that from the single bar model. We attribute this difference to the nodal geometry: the polymer accumulates large shear strain in the nodal region of this stubby sample, which results in higher loss than predicted by single bar simulations. Figure 6 depicts the maximum principal strain in the polymeric layer of samples A and B from single bar and unit cell simulations: the nodal strain is clearly higher in sample B than in sample A.

Altogether, the results of the FE simulations confirm that the analytical model predicts the single bar behavior accurately when the total wall thickness is small relative to the diameter. Furthermore, when it comes to the unit cell level, although the analytical model shows some discrepancies in predicting the storage modulus, the trend of the discrepancies is the same as in single layer lattices [32]. The model predicts the damping accurately when ℓ/D is large and the node is small relative to the whole unit cell (sample A) but is underpredicting when ℓ/D is small and the node is large relative to the whole unit cell (sample B). As our goal is to

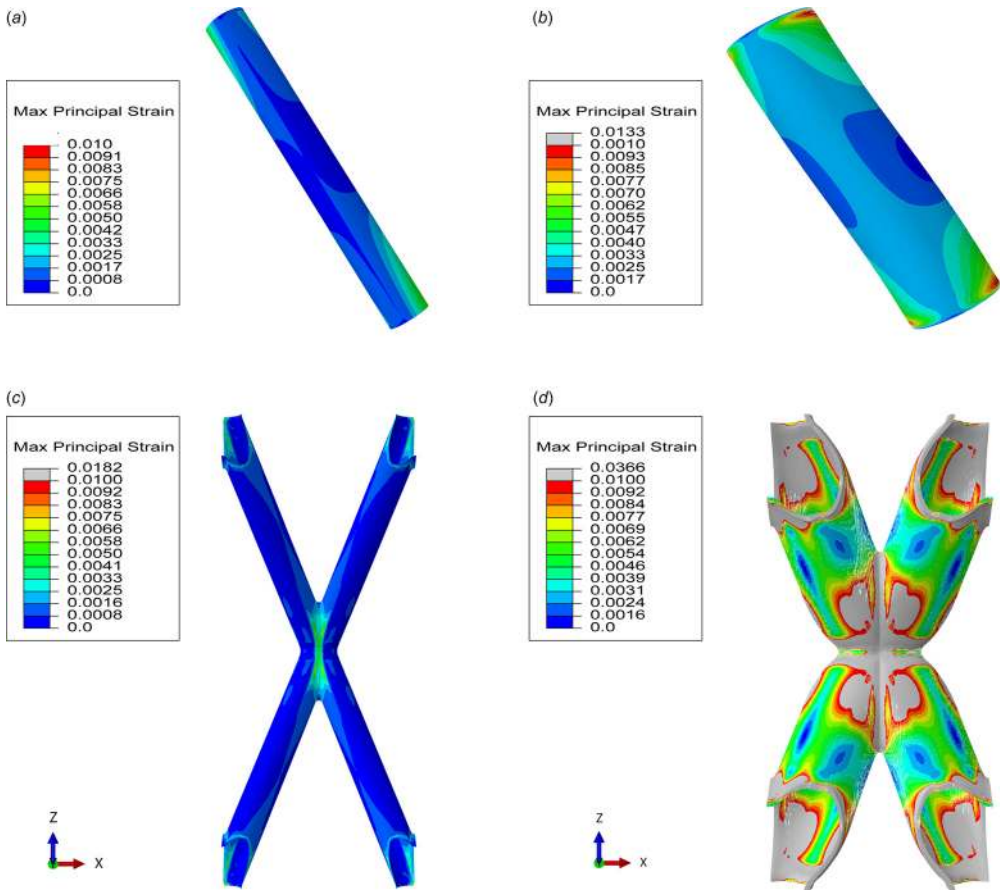

Fig. 6 Maximum principal strain in the TPU layer under lattice compression: (*a, b*) single bar analysis and (*c, d*) unit cell analysis. Results are provided for sample A (*a, c*) and sample B (*b, d*).

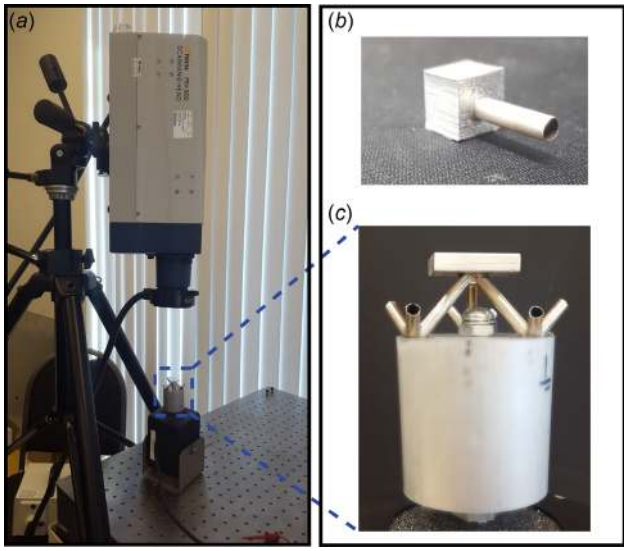

Fig. 7 (*a*) Laser Doppler vibrometer (PSV-500), (*b*) single bar in cantilever mode, and (*c*) single unit cell under uniaxial loading

design lattices with highest damping coefficient based on the analytical model (Sec. 4), the implication is that the optimization results will always be conservative.

3.3 Experimental Verification of Constrained-Layer Damping. Resonance measurements at infinitesimal strains are performed to capture the constrained-layer (intrinsic) damping in two different configurations: (i) on a single bar loaded in cantilever mode and (ii) on an individual unit cell. The single bar measurement is used to investigate the accuracy of the analytical model and the single unit cell measurement helps understanding the effects of the nodes on constrained-layer damping. A half-layer tetrahedral lattice was fabricated as described in Sec. 2. The tetrahedral configuration was chosen for ease of fabrication. For the sake of model validation, the analytical models in Sec. 3.1 are appropriately modified to represent the tetrahedral configuration. Clearly, the results of these comparisons can be applied to the octahedral lattices as well, as both have the same dissipation mechanisms. All experiments are carried out with a laser Doppler vibrometer (PSV-500, Polytec GmbH, Irvine, CA) depicted in Fig. 7(*a*).

A single bar is extracted from the lattice and press-fitted to the aluminum base to create a fixed boundary condition (cantilever bar) as depicted in Fig. 7(*b*). The bar is assembled on top of a shaker (Labworks Inc., Costa Mesa, CA, ET-132-2) by using mounting wax (PCB, Piezotronics, Petro wax). The aluminum base is oscillated via a shaker with a fast Fourier transform sinusoidal signal at very low amplitude (~0.01 μm), sweeping the frequency within the range of 0–15 kHz. The velocity of the aluminum base and hybrid bar is monitored with the Doppler vibrometer in scanning mode (to identify the modal shapes).

The response of the base plate and the bar are depicted in Figs. 8(*a*) and 8(*b*), respectively. An out-of-plane axial mode for the aluminum base was detected at ~13 kHz. To eliminate the effects of base excitation, a transfer function $H1 = (Y(\omega)/X(\omega))$ is used, with $X(\omega)$ being the average deflection of the base and $Y(\omega)$ the deflection of individual points on the bar with respect to the $X(\omega)$ excitation. The frequency response of every single point on the bar is calculated by using the above transfer function and the response of a single point is depicted in Fig. 8(*c*).

As Fig. 8(*c*) indicates, two modes are coupled at a frequency of ~12 kHz. The combined mode has the appearance of the first bending mode (inset in Fig. 8(*c*)). A Gaussian function is used to decouple these modes from each other and the result is depicted in Fig. 9.

Two different methods can be used to capture the damping of the structure from the resonance response: (i) the half bandwidth method and (ii) the structural damping method. In the first method, the loss factor η is extracted from the ratio of the resonance peak width (measured at an amplitude of $1/\sqrt{2}$ of the peak amplitude) to the resonance frequency [37]. In the second method, the equation of motion is written as

$$m\ddot{x}(t) + k^*x(t) = F(t) \tag{5}$$

where m is the mass of the system, $k^* = k' + ik$ is the stiffness of the structure and the harmonic excitation which was applied to the structure can be expressed as $F(t) = Ake^{i\omega t}$. Equation (5) can be reduced to

$$\ddot{x}(t) + \omega_n^2(1 + i\tan\delta)x(t) = \omega_n^2 Ae^{i\omega t} \tag{6}$$

where $\omega_n = \sqrt{k/m}$ is the natural frequency and $\tan\delta$ is the damping coefficient. The specific solution to Eq. (6) is

$$x(t) = \mathrm{Re}[AG^*(\omega)e^{i\omega t}] = A \cdot |G^*(\omega)| \cdot \cos(\omega t - \phi^*) \tag{7}$$

where

$$\left|G^*(\omega)\right| = \frac{1}{\left\{\left[1 - (\omega/\omega_n)^2\right]^2 + \tan^2\delta\right\}^{1/2}} \tag{8}$$

To calculate the damping coefficients $\tan\delta$ and the corresponding natural frequencies ω_n, Eq. (8) was fitted on the experimentally measured frequency response curve.

For the sample in our test, both methods generate identical results. Figure 10 shows the results of the curve fit method on two

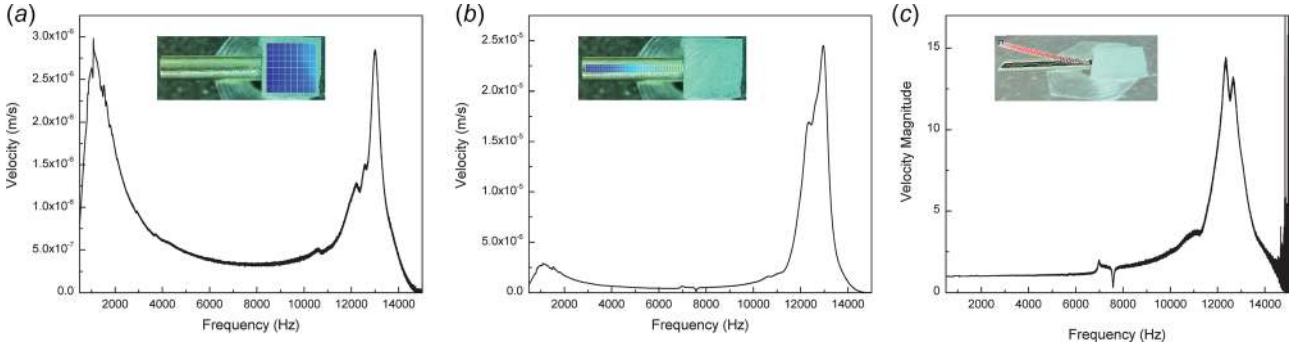

Fig. 8 Frequency response of (*a*) aluminum base, (*b*) hybrid bar, and (*c*) hybrid bar with respect to aluminum base excitation by applying H1 transfer function

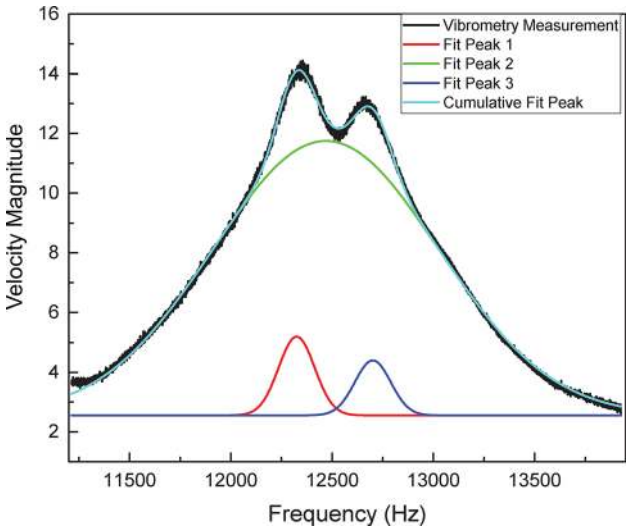

Fig. 9 Decoupling of the first two resonant modes

peaks in Fig. 9. Both peaks show a damping coefficient $\eta = \tan\delta = 0.02$.

Frequency extraction (a.k.a. linear perturbation analysis) is performed on a single bar with the same dimensions as tested bar (see Sec. 2 for dimensions) in finite elements simulations performed with ABAQUS/STANDARD. The thickness of the polymer is swept between $t_p = 4.7 - 30\,\mu$m to capture the effects of the polymer layer on the natural frequencies of the single bar. The four lowest vibration modes and corresponding eigenfrequencies are obtained via eigenvalue extraction. In the sample with $t_p = 4.7\,\mu$m, the first and the second modes are cross section pinching modes with identical frequencies of ~10 kHz; the third mode and the fourth modes are first in-plane and first out-of-plane bending modes, respectively, with identical frequencies of ~13 kHz. By increasing the polymer layer thickness, the first and the second modes are switching with the third and the fourth modes, and the frequencies of the bending modes are decreasing. Therefore, we conclude that the two bending modes (in-plane and out-of-plane) captured in the FE simulations are actually the two coupled modes in the experiment. The difference in the frequencies of these two modes is attributed to manufacturing defects (e.g., nonuniformity of the polymer layer).

We can predict the damping coefficient of the hybrid bar with the model developed in Sec. 3.1. Note that the damping coefficient of the hybrid bar is measured at ~13 kHz (resonance peak), while the damping coefficient of TPU is obtained via dynamic mechanical analysis at 1 Hz. Macaloney et al. [38] have reported the frequency dependence of TPU (albeit at low temperature, −61C) over a frequency range of 20 orders of magnitude. From 1 Hz to 10,000 Hz, the damping coefficient of TPU reduces by half. Hence, we use a value of $\tan\delta = 0.1$ for the polymer (~2× lower than measured experimentally) to predict the damping coefficient of the hybrid bar at high frequency. With these material properties, the analytical model (modified for tetrahedral lattices) predicts a damping coefficient that varies between $\eta = 1.1 \times 10^{-4}$ and 0.0035 when the polymer layer thickness is swept from $t_p = 4.7$ to 100 μm. Hence, the model underpredicts the damping coefficient by at least a factor of 4 (in the experiment, $\eta \sim 0.02$). In the analytical model, the entire damping is due to the viscoelastic nature of the polymeric layer. However, a previous study on damping of nickel hollow microlattice materials [29] revealed that the nickel structure shows non-negligible intrinsic damping as well. To isolate the effect of the metal layer, a single layer nickel bar with the same length, diameter, and metallic wall thickness as the hybrid bar is tested under the same conditions. The extracted damping coefficient for the single layer nickel bar is $\eta = 0.0155$ for the first bending mode. The difference between the damping of the hybrid bar and that of the nickel bar (which can be attributed entirely to the effect of the polymer) is ~0.0035, which is within the range of analytical model prediction for polymer thickness in the range $t_p = 4.7 - 100\,\mu$m.

A similar experiment is performed on a single half unit cell (Fig. 7(*c*)). The sample is extracted from the hybrid microlattice and bonded to two aluminum face sheets. The bottom face sheet is a 5-cm-thick aluminum rod (chosen based on FE simulations to avoid any eigenmodes below the resonance frequency of the lattice) and the top face sheet is a 20 mm × 20 mm × 4 mm plate, which is ~10x heavier than the lattice (Fig. 7(*c*)). The bottom plate is excited via a shaker with frequencies within the range 0–10 kHz, while the top and bottom plates are scanned by laser Doppler vibrometry. The curve fit method is used to extract a damping coefficient $\eta = 0.018$ (Fig. 11(*a*)).

The same procedure is repeated for a nickel half unit cell lattice and the damping coefficient is extracted (Fig. 11(*b*)). The damping coefficient of the nickel hollow microlattice is $\eta = 0.015$. The difference between the intrinsic damping of the hybrid half unit cell and that of the nickel half unit cell is ~0.003, which is once again within the range predicted by the analytical model.

Overall, these experiments reveal that adding a layer of TPU within the metallic wall of a hollow microlattice increases its

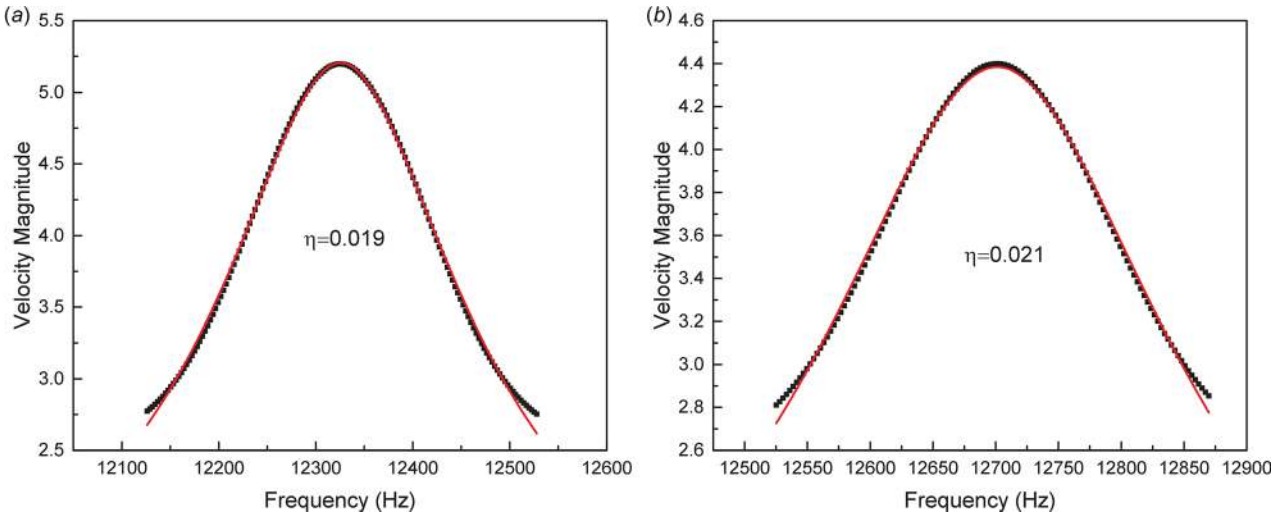

Fig. 10 Damping coefficients extracted from the frequency response (measured by laser Doppler vibrometry) using the curve fit method for a single hybrid bar: (*a*) first mode and (*b*) second mode

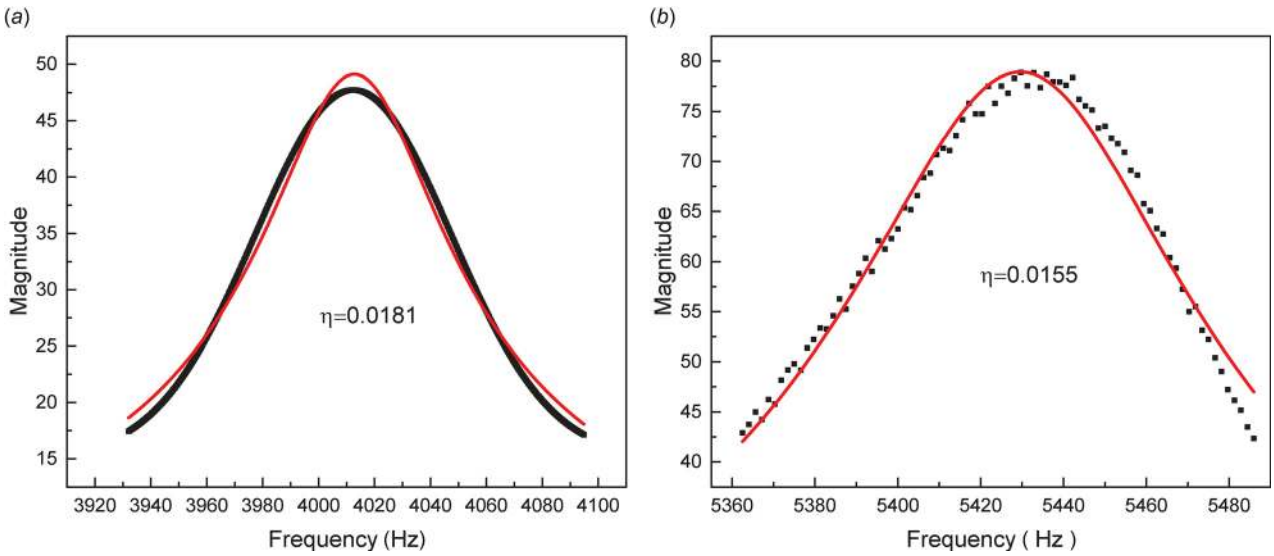

Fig. 11 Damping coefficient of (*a*) hybrid tetrahedral half unit cell and (*b*) a nickel tetrahedral half unit cell with the same geometry, extracted from the frequency response (measured by laser Doppler vibrometry)

damping coefficient by ~20%. It is worth mentioning that for this specific lattice, the damping coefficients of a single bar and half unit cell are very close; however, our FE simulations suggest that the damping coefficient can be further increased by stacking up several unit cells due to nodal effects.

4 Structural Damping Analysis

The mechanical response of hollow metallic lattices under uniaxial compression has been thoroughly investigated in previous studies [25,28–31]. These lattices show vastly different behavior depending on their relative density: (1) For relative densities higher than a critical value (for Nickel lattices, $\bar{\rho} \sim 0.1\%$), the typical cellular metal behavior is observed, with a linear elastic region followed by an extensive plastic deformation plateau, resulting in no reversibility upon unloading. (2) Conversely, for relative densities lower than this critical value (ultralight lattices), a unique pseudo-super-elastic behavior is observed whereby full recoverability is achieved upon very large straining (in excess of 50%). This recoverability is associated with a very large hysteresis cycle, resulting in very large damping. Salari-Sharif et al. [29] thoroughly investigated this damping behavior and showed that the largest amount of energy loss occurs via local elastic buckling of the bars and the associated vibration and heat generation, a unique form of structural damping.

The same qualitative behavior is expected for hybrid hollow lattices. When designed below a critical density, ultralight hybrid lattices can then exhibit two distinct damping mechanisms: the constrained-layer damping investigated in Sec. 3 and the structural damping mechanism associated with local buckling of the bars. Clearly, the latter only applies to loading conditions where the lattice is subjected to large strain amplitudes (required to induce buckling of a significant number of bars), whereas the former applies to deformations with infinitesimal strain amplitudes. In this section, we extend a previously derived analytical model for structural buckling to hybrid lattices.

This structural damping mechanism can be clearly elucidated with a simple FE simulation of a single hollow hybrid bar (for the purpose of this demonstration, we choose a diameter of 1 mm, a length of 4 mm, a polymer wall thickness of 100 nm, and a nickel wall thickness of 538 nm). A very similar simulation (albeit conducted on a simple metallic hollow bar) was conducted in Ref. [29]. The details of the simulation are repeated here for completeness. The bar is loaded in cantilever mode (Fig. 12(*a*)), whereby one edge is fixed, while the other edge is allowed to move in all directions (albeit as a rigid body) but not allowed to rotate. Moreover, the cross section is kept circular during the entire simulation. To address convergence issues, a dynamic simulation is performed in ABAQUS/EXPLICIT under displacement control, with the application and subsequent removal of an end displacement of 200 μm. In order to ensure negligible inertia effects, a very small displacement rate is chosen (0.2 m/s), and the kinetic energy is monitored to guarantee that the kinetic energy be very small compared to the elastic energy during the entire simulation. Additionally, a smooth function for displacement, namely a polynomial function in which the first and second derivatives are zero at the initial and final amplitudes, was used to ramp up or down smoothly from one amplitude value to another amplitude value and to prevent sudden shocks at the beginning of the simulation. Both materials are modeled as elastic perfectly plastic, with material properties as defined in Sec. 3.2 and yield strength of 2.5 GPa and 26 MPa for nickel and TPU, respectively. Since we are not interested in capturing viscous damping in this simulation, no viscoelastic properties are introduced. The model is meshed with a four-node reduced integration shell element (S4R), with hourglass control and finite membrane strain. During the simulation, the beam undergoes large post-buckling deformation; hence, a self-contact (hard, frictionless) constraint is enforced along the entire cylinder.

Figure 12(*a*) shows the von Mises stress contours on the metallic layer in the deformed bar at the end of the loading cycle, while Fig. 12(*b*) depicts the force–displacement response in the entire cycle. The bar behaves linearly up to a displacement of ~25 μm, after which local buckling occurs near the clamped end, resulting in an instantaneous and dramatic load drop. In the post-buckling response, the bar exhibits nearly linear elastic behavior, albeit with much reduced stiffness. Upon unloading, the bar initially follows the post-buckling loading curve past the buckling point, after which it snaps back to the prebuckling curve. The shaded area in Fig. 12(*b*) represents the dissipated energy during the simulation, which in a practical scenario would be converted to heat.

Of course, this energy dissipation mechanism can only occur if the bars remain elastic upon local buckling and subsequent folding about the creases. This constraint can be expressed in the form of a maximum wall thickness to diameter ratio, as explained in detail in Refs. [29] and [30]. For hybrid lattices, this constraint takes the following form:

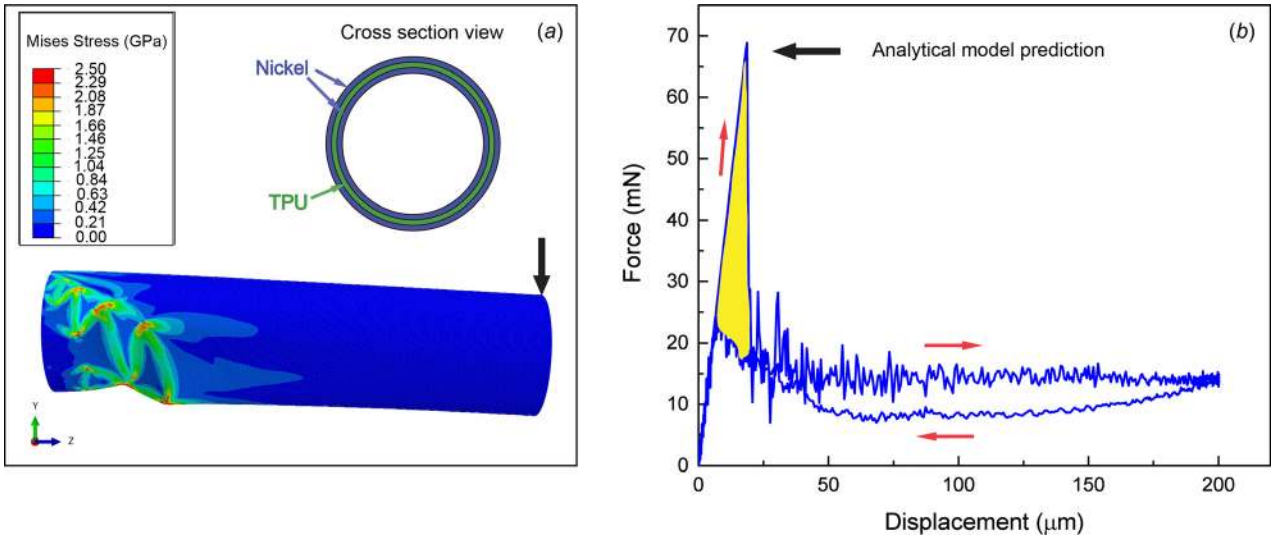

Fig. 12 (*a*) The deformed shaped of hybrid hollow cantilever bar captured by FE simulations. The contours show the Mises stress distribution in the metallic layer. (*b*) Force–displacement curve for a loading–unloading cycle, with the shaded area representing the energy dissipated in one cycle.

$$\frac{t_m^i + t_m^o}{D} < \frac{0.25}{\theta - \sin^{-1}((1-\varepsilon_{\max})\sin\theta)} \cdot \frac{\sigma_m}{E_m} \tag{9}$$

where σ_m is the yield strength on the metal layer and $\varepsilon_{\max}$ is the maximum compressive strain from which the lattice is expected to recover. The geometrical dimensions are defined in Fig. 2.

In a bulk lattice under compression, a large number of bars can dissipate energy through this mechanism. The energy dissipated by the entire lattice in a cycle is roughly given by the sum of these contributions for all the bars that buckle. This energy dissipation can be approximately modeled using classic local buckling theory. In previous work, the same behavior had been observed for ultralight nickel hollow microlattice materials, with remarkable agreement between the experimental data and a simple analytical model [29]. This model can be easily extended to hybrid lattices as discussed below.

Upon uniaxial compression of a lattice, each bar experiences a combination of axial compression, bending moment, and transverse shear, as indicated in Fig. 4. Neglecting the stresses induced by the shear load relative to those induced by the axial and bending moment, and ignoring the load carrying capacity of the polymeric layer, the maximum normal compressive stress $\sigma_{\max}$ experienced by the metal layer in the bar wall can be expressed as

$$\sigma_{\max} = \frac{P}{4\pi D\left(t_m^i + t_m^o\right)}\left(\sin\theta + \frac{2\ell}{D}\cos\theta\right) \tag{10}$$

where P is the compressive load applied on a single unit cell (Fig. 4). The bar buckles when the maximum stress in the bar reaches to the critical local buckling stress; buckling occurs near the bar end, where the moment is maximum. The local buckling stress for sandwich-wall hollow cylinders with small polymer wall thickness to diameter ratio can be written as [39]

$$\sigma^{lb} = \frac{2E_m}{\sqrt{1-\upsilon_m^2}}\frac{r_g}{R} \tag{11}$$

where

$$\frac{r_g}{R} = \frac{t_p + t_m}{D}\sqrt{1 + \frac{1}{3}\left(\frac{t_m}{t_p + t_m}\right)^2} \tag{12}$$

and E_m and ν_m are, respectively, Young's modulus and Poisson's ratio of the metal layer. (We assume that the inner and outer metal skins have the same thickness, i.e., $t_m^i = t_m^o = t_m$.) By equating Eqs. (10) and (11), the buckling strength of a single hybrid hollow bar loaded as described earlier (which is equal to one-quarter of the strength of the unit cell) can be expressed as

$$P_{\text{bar}}^{\text{lb}} = \frac{P_{\text{cr}}}{4} = \frac{2\pi E_m D^2 t_m}{\sqrt{1-\nu^2}\,\ell\cos\theta\left(1 + \frac{D}{\ell}\frac{\tan\theta}{2}\right)}\left(\frac{r_g}{R}\right) \tag{13}$$

This model was verified by the FE simulation (Fig. 12(*b*)). The FE simulation predicts a critical buckling load of 64.4 mN versus an analytically predicted value of 66.6 mN.

The stiffness of a single bar within the unit cell (equal to one half of the stiffness of the entire cell) can be computed analytically by equating the external work of deformation to the internal strain energy induced by the moment, axial load, and shear load (as explained in Sec. 3.1), leading to

$$K_{\text{bar}} = \frac{K}{2} = \frac{3\pi D^3 t_t E_{\text{voigt}}^*}{2\ell^3\cos^2\theta}\left(1 + \frac{3}{2}\left(\frac{D}{\ell}\right)^2\tan^2\theta + 3\frac{E_{\text{voigt}}^*}{G_p}\frac{t_t}{t_p}\left(\frac{D}{\ell}\right)^2\right) \Bigg/ \left(1 + \frac{t_m^i + t_m^o}{t_p}\frac{G_m}{G_p}\right)^{-1} \tag{14}$$

Although in Sec. 3.1 the modulus of the polymer was treated as a complex number to capture its viscoelastic nature, here we only consider its magnitude.

The elastic energy dissipated in each bar upon local buckling can be approximated by

$$\Delta E_{\text{bar}} = \frac{P_{\text{bar}}^{\text{lb}2}}{2K_{\text{bar}}} \tag{15}$$

The bulk lattice contains n_x, n_y, and n_z cells along the X, Y, and Z directions, respectively. As each unit cell has 16 bars, the total number of bars in the bulk lattice is given by $N_b = 16n_xn_yn_z$. The dimensions of the lattice can be derived from the geometry of the bar and the number of unit cells in the lattice as $L = 2\ell\cos\theta n_y$,

$H = 2\ell \sin\theta n_z$, and $W = 2\ell \cos\theta n_x$, where L, H, and W are, respectively, the length, height, and width of the unit cells. Finally, the dissipated energy in the structure can be modeled via a simple energy balance as

$$\Delta U = \frac{N_b f \Delta E_{\text{bar}}}{WHL} = \frac{2f\Delta E_{\text{bar}}}{\ell^3 \sin\theta \cos^2\theta} \tag{16}$$

where f is the fraction of bars that need to buckle in order to accommodate the global lattice strain. A simple estimate for f at a maximum applied strain $\varepsilon_{\max}$ can be found by assuming layer-by-layer deformation and complete folding of each bar onto itself upon buckling

$$f = \frac{\varepsilon_{\max}}{1 - D/(\ell \sin\theta)} \tag{17}$$

5 Trends for Optimal Design

The mechanical models for constrained-layer damping and structural damping described in Secs. 3.2 and 4, respectively, can be adopted in optimization studies to identify the optimal response and generate optimal design maps. Two optimization studies will be discussed in this section: (1) Maximization of the damping figure of merit $|E^*|^{1/3}\tan\delta/\rho$, where damping is induced by the viscoelastic nature of the polymer (modeled in Sec. 3.2). (This figure of merit expresses how fast a clamped plate subject to forced vibrations reaches the rest state when the forcing term is removed.) (2) Maximization of the energy dissipated in a compression cycle (ΔU), where the dissipation originates from structural damping (modeled in Sec. 4).

5.1 Maximization of Intrinsic Damping Through Figure of Merit $|E^*|^{1/3}\tan\delta/\rho$. The geometric parameters of the system are expressed in nondimensional form as follows: the truss angle (θ), the bar aspect ratio (D/ℓ), the ratio of the metallic layer thickness to the bar length (t_m/ℓ), and the ratio of the polymeric layer thickness to the bar length (t_p/ℓ). The objective function is $|E^*|^{1/3}\tan\delta/\rho$ where $|E^*|$, $\tan\delta$, and ρ are given by Eqs. (1), Eq.(3), and Eq. (4), respectively. The following constraints are added to the optimization study to express the manufacturing and beam theory limitations:

$$\begin{aligned} &10^{-3} < D/\ell < 0.25 \\ &2 < L/D < 16 \\ &10^{-4} < t_m/\ell < 0.3 \\ &10^{-4} < t_p/\ell < 0.3 \\ &45^\circ < \theta < 75^\circ \end{aligned} \tag{18}$$

where $L = 2\ell\cos\theta$ is the cell size. To avoid converging to solutions with excessive amount of polymer (that would not be manufacturable with the process described in Sec. 3), the additional constraint $t_p/t_m < 10$ is included.

The constrained optimization problem is solved with the MATLAB "fmincon" algorithm, for lattice densities ranging between 10 and 1000 kg/m^3.

To elucidate the effects of the viscoelastic properties of the polymeric layer (modulus and damping coefficient) on the lattice performance, the optimization problem is solved with ten different polymers, all with $|E^*|\tan\delta = 10^8$. Young's modulus is varied from 100 MPa to 50 GPa and the damping coefficient from 0.002 to 1.

The performance of optimal hybrid lattices is presented as a plot of the material index ($|E^*|^{1/3}/\rho$) versus the loss coefficient ($\tan\delta$) in Fig. 13(*a*); the optimal dimensions are shown in Figs. 13(*b*)–13(*d*). Results for only four polymer choices are presented to avoid overcrowding the figures.

For all material combinations, the maximum value of the figure of merit (indicated by the dashed selection line in Fig. 13(*a*)) is achieved for the lightest designs. As the density is increased from its lowest value, initially t_p/ℓ and t_m/ℓ remain constant, while the truss angle θ and D/ℓ increase, resulting in a decrease in the figure of merit. When the truss angle θ and D/ℓ reach their upper bounds, t_p/ℓ and t_m/ℓ start increasing; in this phase, the figure of merit is still decreasing, but at a slower rate. The constraint $t_p/t_m < 10$ is active over the entire range of densities, and for all material combinations. Notice that the optimal dimensions are essentially identical for all choices of polymer, and very similar values of the figure of merit are achieved with different polymers. The effect of the polymeric layer material can be appreciated if the three properties in the figure of merit are separated. Young's modulus versus density and Young's modulus versus loss factor for the same optimization results are depicted in Fig. 14.

Clearly, polymers with higher Young's modulus lead to hybrid lattices with higher Young's modulus as well although the effect is rather small. Interestingly, though, the effect of the polymer loss factor is less obvious. For relatively small polymer loss factor ($\tan\delta < 0.1$), increasing the loss factor of the polymer results in a lattice with higher loss factor; but at higher polymer loss factors ($\tan\delta > 0.1$), the effect is reversed. This reversal is due to the fact that the polymeric layer must possess sufficient stiffness in order to dissipate a meaningful amount of strain energy: very lossy polymers are too compliant to dramatically affect the response of the lattice. Hence, Fig. 14 can be used as a design selection map: once the desired loss coefficient of the lattice is chosen, Fig. 14(*b*) can be used to identify suitable polymers; subsequently, the density (and hence all the geometric parameters) can be chosen from Fig. 14(*a*) to design a lattice with a desired Young's modulus.

If the optimization study is performed without enforcing the $t_p/t_m < 10$ constraint, the optimal lattices have higher damping coefficient and lower Young's modulus (due to the tendency toward thicker polymer layer and thinner nickel layer); clearly, those lattices are more challenging to manufacture.

The results indicate that the maximum achievable damping coefficient for the lattice is equal to that of the polymeric layer (as long as the $t_p/t_m < 10$ constraint is not included); however, the stiffness of the lattice would always exceed the stiffness of the polymeric layer.

In order to clearly quantify the mechanical advantages of hybrid lattices over single material lattice, optimal nickel/TPU/nickel lattices are compared to optimal single material lattices made of either nickel or TPU (Fig. 15). The performance of nickel/TPU Reuss and Voigt composites, bulk nickel and bulk TPU are added for reference. The mechanical properties of nickel and polymer layer were given in Sec. 2. The densities of all the lattices are swept in the range 10–1000 kg/m^3 and the densities of both Voigt and Reuss composites are swept in the range 1200–8900 kg/m^3. Results for hybrid lattices are presented for two different t_p/t_m constraints ($t_p/t_m < 10$ and $t_p/t_m < 25$), in order to better understand the effects of manufacturing constraints and the advantages of allowing thicker polymeric layers. The specific stiffness index ($|E^*|^{1/3}/\rho$) is cross plotted against the loss factor in Fig. 15(*a*), allowing identification of materials with optimal values of the damping figure of merit $|E^*|^{1/3}\tan\delta/\rho$. Clearly, the single-material TPU lattice is superior on this metric, whereas the single-material nickel lattice is the worst. Hybrid lattices have intermediate performance and they are generally superior to fully dense Reuss and Voigt composites. Allowing thicker polymeric walls results in higher lattice loss factor, with a small penalty in specific stiffness. To fully appreciate the benefits of hybrid lattices, though, it is instructive to plot Young's modulus against the density (Fig. 15(*b*)). Clearly, all lattices can be much lighter than the fully dense Voigt and Reuss composites, with hybrid lattices almost approaching the stiffness of nickel lattices for densities

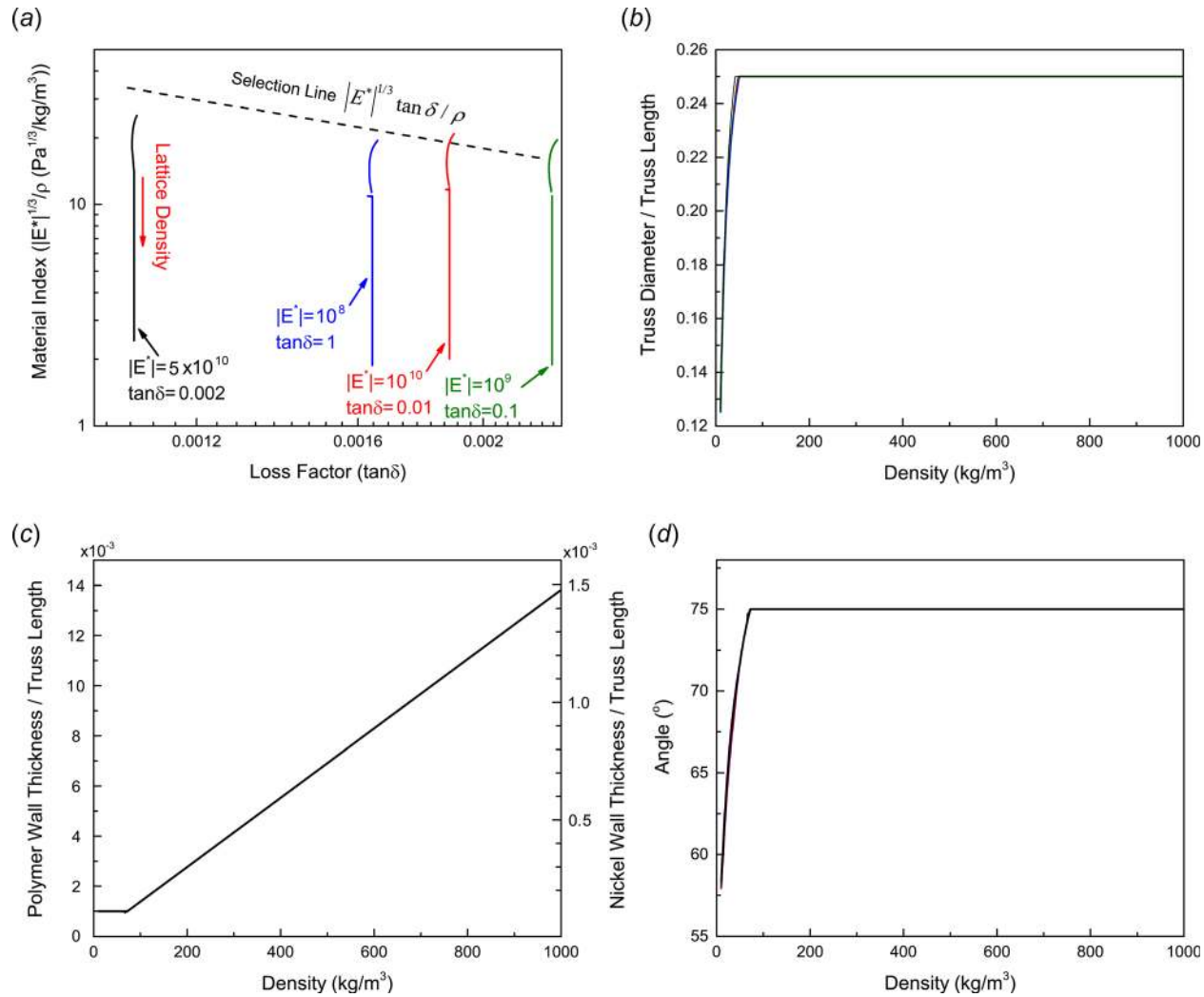

Fig. 13 (*a*) Map of achievable $|E^*|^{1/3} \tan \delta/\rho$ of hybrid microlattices with four different polymers and ((*b*)–(*e*)) optimal lattice dimensions, which are essentially identical for all polymers

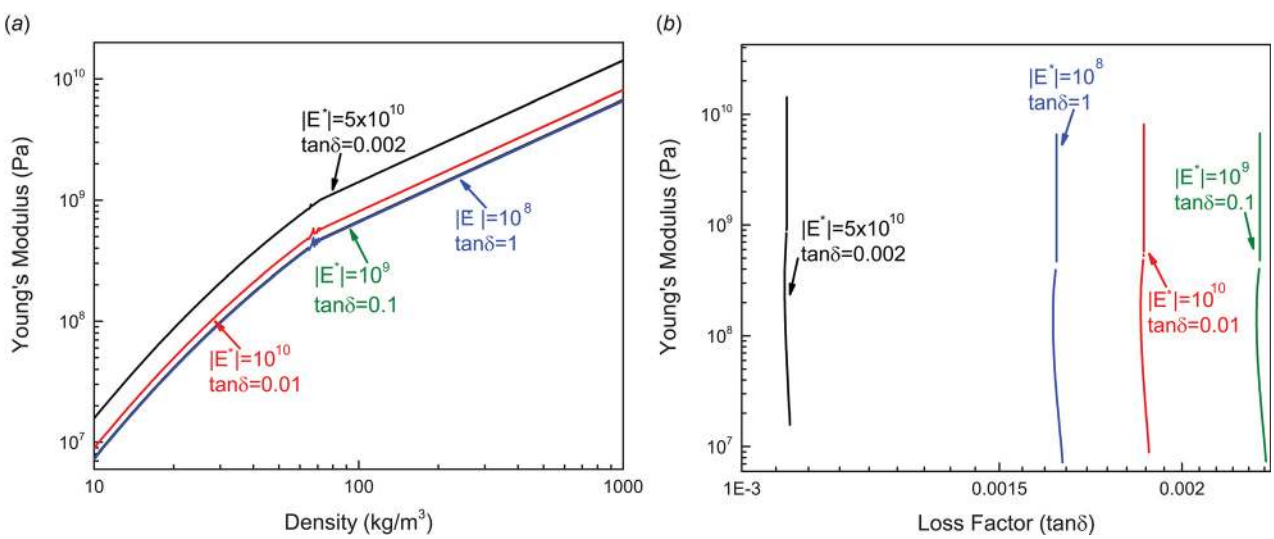

Fig. 14 Young's modulus versus (*a*) density and (*b*) loss factor for hybrid hollow microlattices with four different polymers

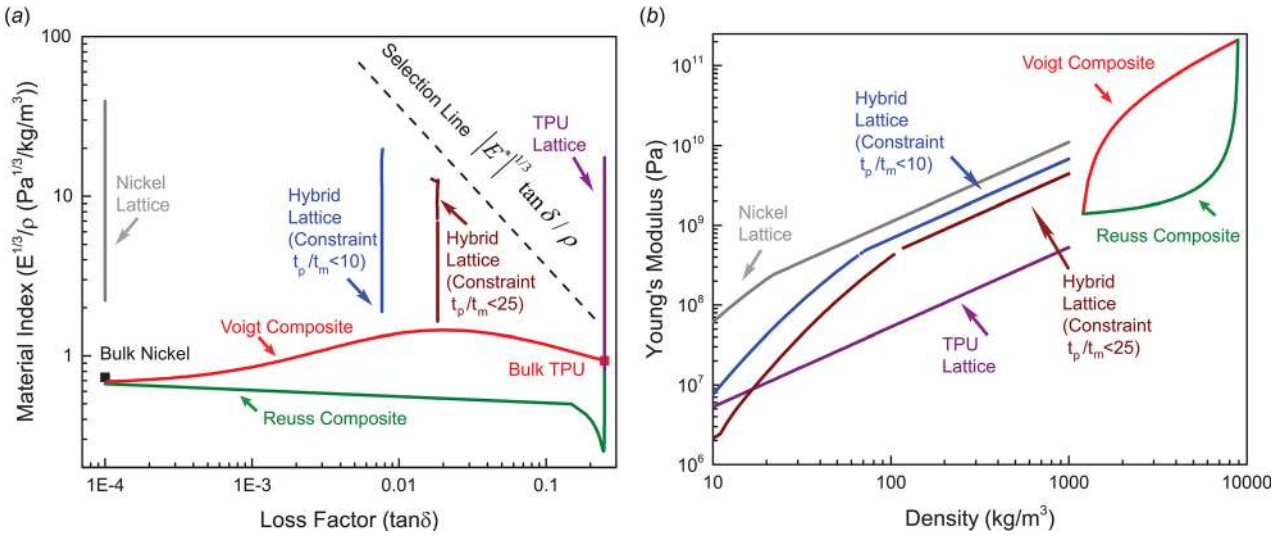

Fig. 15 (*a*) Material index ($|E^*|^{1/3}/\rho$) versus loss factor and (*b*) Young's modulus versus density, comparing bulk nickel, bulk TPU, nickel microlattice, TPU microlattice, Reuss composite, Voigt composite, and hybrid microlattices with two different constraints ($t_p/t_m < 10$ and $t_p/t_m < 25$)

larger than ~100 kg/m^3. The conclusion is that hybrid hollow lattices can be designed with stiffness comparable to that of metallic hollow lattices, but with loss factors two orders of magnitude higher.

5.2 Maximization of Structural Damping Through Dissipated Energy Per Cycle, ΔU. In this section, we design lattices that maximize energy dissipation emerging from the buckling-induced structural damping discussed in detail in Sec. 4. As a reminder, unlike the constrained-layer damping discussed in Sec. 3, this damping mechanism is only observable in ultralight lattices (both hybrid and single-material). This condition is imposed in the form of a recoverability constraint (Eq. (9)), which effectively limits the thickness to diameter ratio. The other dimensional constraints are the same as those for the previous problem (Eq. (18)).

For ultralight metallic lattices, the recoverability constraint (Eq. (9)) automatically guarantees that buckling precede yielding. The same is not rigorously true for hybrid lattices. Hence, we also request that

$$\frac{P^{\text{lb}}_{\text{bar}}}{P^{y}_{\text{bar}}} < 0.9 \tag{19}$$

where $P^{\text{lb}}_{\text{bar}}$ is the critical local buckling load of a single bar derived from Eq. (13) and P^{y}_{bar} is the yielding load of a single bar, calculated as

$$P^{y}_{\text{bar}} = \frac{\pi D^2 t_m \sigma_y}{\ell \cos\theta\left(1 + \frac{D}{\ell}\frac{\tan\theta}{2}\right)} \tag{20}$$

The coefficient 0.9 is chosen to provide some level of conservatism.

The constrained optimization problem described previously is solved with the "fmincon" algorithm in MATLAB for densities in the range 10–200 kg/m^3.

Figure 16 shows the dissipated energy per cycle as a function of the density for optimal hybrid lattices constructed with ten different polymers (as described in Sec. 5.1, all polymers have the same value of $|E^*|\tan\delta = 10^8$). As before, nickel is used as the metal layer for all lattices. The maximum amounts of dissipated energy for four polymer choices are shown in Fig. 16 to avoid overcrowding the figures, whereas the optimal dimensions are detailed in Fig. 17.

The key conclusion is that adding a polymer inner layer to a metallic wall in an ultralight hollow lattice increases the energy dissipation related to this structural damping mechanism by ~6–8 times. This is due to an increase in the local buckling load provided by the sandwich construction of the bar walls. Such increase, however, varies only slightly for polymers with different properties. In fact, there is only a 15% difference between the increase in energy dissipation yielded by using the polymers with the lowest damping coefficient and the polymer with the highest damping coefficient. This is because the critical buckling load of the hybrid lattice is a strong function of the stiffness of the metal layer and the geometry of the lattice, and is largely unaffected by the properties of the polymeric layer. However, note that, as detailed in Sec. 5.1, the polymer with higher damping coefficient yields higher constrained-layer viscous damping (for polymers with $\tan\delta < 0.1$), and hence, higher overall damping at the lattice level.

Comparing the optimal lattice dimensions captured from optimizing the constrained-layer damping (Figs. 13(*b*)–13(*e*)) and the

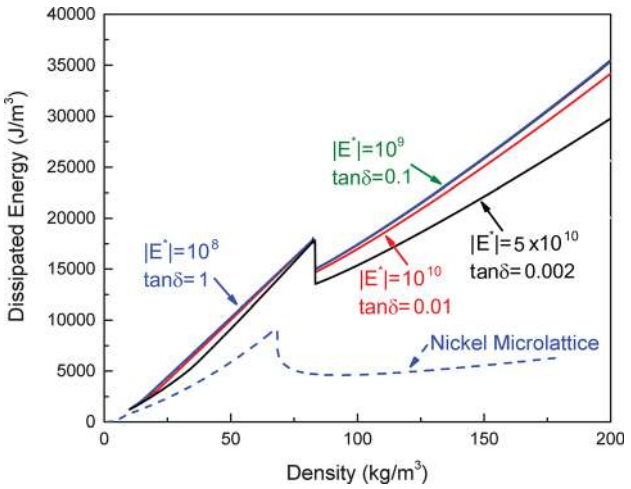

Fig. 16 Map of achievable dissipated energy in hybrid microlattices for the four different polymers, compared to nickel microlattices

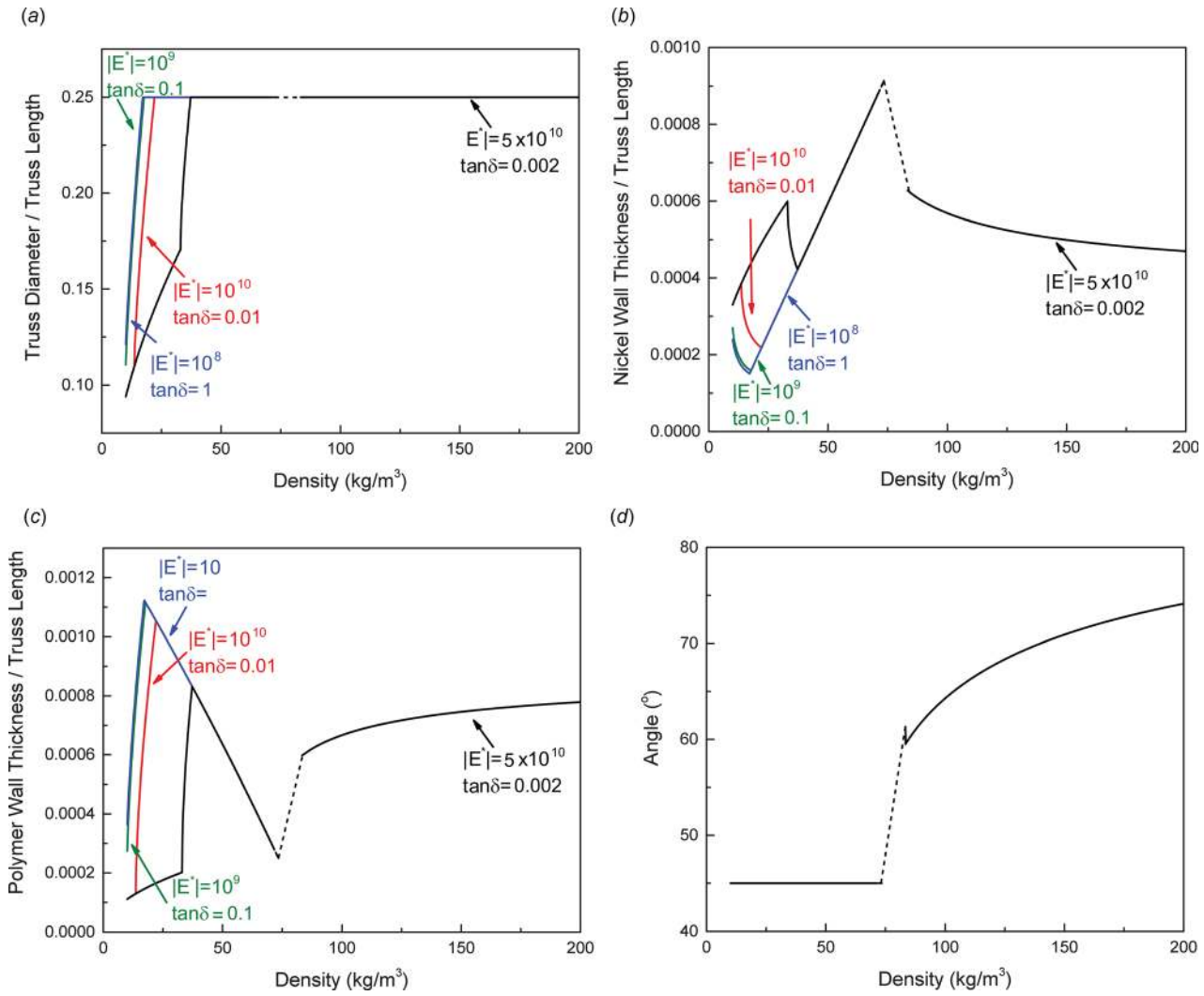

Fig. 17 Optimal dimensions for hybrid lattices that maximize dissipated energy, ΔU

structural damping (Fig. 17) mechanisms clearly reveals that the two optimal dimensions are completely different from each other. The unfortunate implication is that designing an ultralight hybrid lattice which is simultaneously optimized for constrained-layer damping and structural damping does not appear possible.

6 Conclusions

Hybrid hollow microlattices with metal/polymer/metal sandwich walls are fabricated with an extremely scalable additive manufacturing process, and their damping performance is thoroughly investigated. An analytical model is introduced to capture the constrained-layer damping mechanism. The analytical model, which expresses stiffness and damping coefficient as a function of microlattice geometry and materials properties, is validated by finite element simulations and resonance experiments. In the ultralight regime ($\bar{\rho} < 0.1\%$), hybrid hollow microlattices may show recoverability under large compressive strain, due to a mode of deformation characterized by local buckling of the hollow bars. This mechanism—well established for metallic hollow lattices—introduces additional energy dissipation, and can be seen as a unique form of structural damping. Clearly, this damping mechanism is only active when the lattice is subjected to large strain amplitudes. An analytical model for this structural damping mechanism, previously derived for metallic hollow microlattices, is extended to hybrid designs, and validated by finite elements simulations. The model allows estimation of the energy dissipation per unit volume as a function of microlattice geometry and materials properties. Finally, the mechanical models for constrained-layer damping and structural damping are adopted in optimal design studies where the geometric properties of the lattice are optimized for maximum damping figures of merit. The results show that the constrained-layer damping mechanism significantly increases the damping performance of microlattices. Experimental data on a relatively low-density hybrid hollow microlattice sample show an increase in the damping coefficient of ~20% relative to an all-metallic sample of comparable geometry. The improvement is expected to be significantly larger in denser samples which exhibit less structural damping.

An investigation of the role of polymer properties on constrained-layer damping of the lattices reveals that the ideal polymer is not necessarily the lossiest: sufficient stiffness in the polymeric layer is required for efficient damping at the microlattice level. Furthermore, we demonstrate that the presence of the polymer increases the energy dissipation associated with the structural damping mechanism by 6–8× for ultralight lattices ($\bar{\rho} < 0.1\%$). The caveat is that the optimal geometry maps for these optimization studies are significantly different; therefore, in the ultralight regime, we cannot design a single lattice with maximum constrained-layer and structural damping performance. Nonetheless, for situations where both low-strain and high-strain damping are important, the analytical models proposed in this work can be used in optimization studies with more complex figures of merit that combine both damping mechanisms.

Acknowledgment

The authors are indebted to Alan J. Jacobsen and William B. Carter for useful discussions. The ABAQUS® Finite Element Analysis software is licensed from Dassault Systemes SIMULIA, as part of a Strategic Academic Customer Program between UC Irvine and SIMULIA. Ladan Salari-Sharif is grateful to Polytec Inc, specifically Mario Pineda, Jerome Eichenberger, and Eric Lawrence for providing us access to their PSV 500 system and for insightful discussions.

Funding Data

Office of Naval Research (Program Manager: D. Shifler, Contract No. N000141110884).

References

[1] Ashby, F., 2000, *Metal Foams: A Design Guide*, Butterworth-Heinemann Limited, Woburn, MA.
[2] Gibson, L. J., and Ashby, M. F., 1999, *Cellular Solids: Structure and Properties*, Cambridg University Press, Cambridge, UK.
[3] Evans, A. G., Hutchinson, J. W., and Ashby, M. F., 1998, "Multifunctionality of Cellular Metal Systems," Prog. Mater. Sci., **43**(3), pp. 171–221.
[4] Evans, A. G., Hutchinson, J. W., Fleck, N. A., Ashby, M. F., and Wadley, H. N. G., 2001, "The Topological Design of Multifunctional Cellular Metals," Prog. Mater. Sci., **46**(3–4), pp. 309–327.
[5] Banhart, J., 2001, "Manufacture, Characterisation and Application of Cellular Metals and Metal Foams," Prog. Mater. Sci., **46**(6), pp. 559–632.
[6] Rathbun, H. J., Radford, D. D., Xue, Z., He, M. Y., Yang, J., Deshpande, V., Fleck, N. A., Hutchinson, J. W., Zok, F. W., and Evans, A. G., 2006, "Performance of Metallic Honeycomb-Core Sandwich Beams Under Shock Loading," Int. J. Solids Struct., **43**(6), pp. 1746–1763.
[7] Schaedler, T. A., Ro, C. J., Sorensen, A. E., Eckel, Z., Yang, S. S., Carter, W. B., and Jacobsen, A. J., 2014, "Designing Metallic Microlattices for Energy Absorber Applications," Adv. Eng. Mater., **16**(3), pp. 276–283.
[8] Evans, A. G., He, M. Y., Deshpande, V. S., Hutchinson, J. W., Jacobsen, A. J., and Carter, W. B., 2010, "Concepts for Enhanced Energy Absorption Using Hollow Micro-Lattices," Int. J. Impact Eng., **37**(9), pp. 947–959.
[9] Lu, T. J., Valdevit, L., and Evans, A. G., 2005, "Active Cooling by Metallic Sandwich Structures With Periodic Cores," Prog. Mater. Sci., **50**(7), pp. 789–815.
[10] Valdevit, L., Jacobsen, A. J., Greer, J. R., and Carter, W. B., 2011, "Protocols for the Optimal Design of Multi-Functional Cellular Structures: From Hypersonics to Micro-Architected Materials," J. Am. Ceram. Soc., **94**(s1), pp. 15–34.
[11] Lu, T. J., Hess, A., and Ashby, M. F., 1999, "Sound Absorption in Metallic Foams," J. Appl. Phys., **85**(11), pp. 7528–7539.
[12] Luckey, H. A., 1983, *Titanium Alloys in Surgical Implants*, ASTM International, West Conshohocken, PA.
[13] Navarro, M., Michiardi, A., Castaño, O., and Planell, J. A., 2008, "Biomaterials in Orthopaedics," J. R. Soc. Interface, **5**(27), pp. 1137–1158.
[14] Arabnejad Khanoki, S., and Pasini, D., 2013, "Fatigue Design of a Mechanically Biocompatible Lattice for a Proof-of-Concept Femoral Stem," J. Mech. Behav. Biomed. Mater., **22**, pp. 65–83.
[15] Wicks, N., and Hutchinson, J. W., 2001, "Optimal Truss Plates," Int. J. Solids Struct., **38**(30–31), pp. 5165–5183.
[16] Valdevit, L., Hutchinson, J. W., and Evans, A. G., 2004, "Structurally Optimized Sandwich Panels With Prismatic Cores," Int. J. Solids Struct., **41**(18–19), pp. 5105–5124.
[17] Valdevit, L., Pantano, A., Stone, H. A., and Evans, A. G., 2006, "Optimal Active Cooling Performance of Metallic Sandwich Panels With Prismatic Cores," Int. J. Heat Mass Transfer, **49**(21–22), pp. 3819–3830.
[18] Wang, X., and Lu, T. J., 1999, "Optimized Acoustic Properties of Cellular Solids," J. Acoust. Soc. Am., **106**(2), pp. 756–765.
[19] Hammetter, C. I., Rinaldi, R. G., and Zok, F. W., 2013, "Pyramidal Lattice Structures for High Strength and Energy Absorption," ASME J. Appl. Mech., **80**(4), p. 041015.
[20] Banhart, J., Baumeister, J., and Weber, M., 1996, "Damping Properties of Aluminium Foams," Mater. Sci. Eng. A, **205**(1–2), pp. 221–228.
[21] Pritz, T., 1994, "Dynamic Young's Modulus and Loss Factor of Plastic Foams for Impact Sound Isolation," J. Sound Vib., **178**(3), pp. 315–322.
[22] Asadpoure, A., Tootkaboni, M., and Valdevit, L., "Topology Optimization of Multiphase Architected Materials for Energy Dissipation," Comput. Methods Appl. Mech. Eng., **325**, pp. 314–329.
[23] Shan, S., Kang, S. H., Raney, J. R., Wang, P., Fang, L., Candido, F., Lewis, J. A., and Bertoldi, K., 2015, "Multistable Architected Materials for Trapping Elastic Strain Energy," Adv. Mater., **27**(29), pp. 4296–4301.
[24] Haghpanah, B., Salari-Sharif, L., Pourrajab, P., Hopkins, J., and Valdevit, L., 2016, "Multistable Shape-Reconfigurable Architected Materials," Adv. Mater., **28**(36), pp. 7915–7920.
[25] Schaedler, T. A., Jacobsen, A. J., Torrents, A., Sorensen, A. E., Lian, J., Greer, J. R., Valdevit, L., and Carter, W. B., 2011, "Ultralight Metallic Microlattices," Science, **334**(6058), pp. 962–965.
[26] Jacobsen, A. J., Barvosa-Carter, W., and Nutt, S., 2007, "Micro-Scale Truss Structures Formed From Self-Propagating Photopolymer Waveguides," Adv. Mater., **19**(22), pp. 3892–3896.
[27] Jacobsen, A. J., Barvosa-Carter, W., and Nutt, S., 2008, "Micro-Scale Truss Structures With Three-Fold and Six-Fold Symmetry Formed From Self-Propagating Polymer Waveguides," Acta Mater., **56**(11), pp. 2540–2548.
[28] Maloney, K. J., Roper, C. S., Jacobsen, A. J., Carter, W. B., Valdevit, L., and Schaedler, T. A., 2013, "Microlattices as Architected Thin Films: Analysis of Mechanical Properties and High Strain Elastic Recovery," APL Mater., **1**(2), p. 022106.
[29] Salari-Sharif, L., Schaedler, T. A., and Valdevit, L., 2014, "Energy Dissipation Mechanisms in Hollow Metallic Microlattices," J. Mater. Res., **29**(16), pp. 1755–1770.
[30] Torrents, A., Schaedler, T. A., Jacobsen, A. J., Carter, W. B., and Valdevit, L., "Characterization of Nickel-Based Microlattice Materials With Structural Hierarchy From the Nanometer to the Millimeter Scale," Acta Mater., **60**(8), pp. 3511–3523.
[31] Salari-Sharif, L., and Valdevit, L., 2014, "Accurate Stiffness Measurement of Ultralight Hollow Metallic Microlattices by Laser Vibrometry," Exp. Mech., **54**(8), pp. 1491–1495.
[32] Godfrey, S. W., and Valdevit, L., 2012, "A Novel Modeling Platform for Characterization and Optimal Design of Micro-Architected Materials," AIAA Paper No. 2012-2003.
[33] Valdevit, L., Godfrey, S. W., Schaedler, T. A., Jacobsen, A. J., and Carter, W. B., 2013, "Compressive Strength of Hollow Microlattices: Experimental Characterization, Modeling, and Optimal Design," J. Mater. Res., **28**(17), pp. 2461–2473.
[34] Rao, M. D., 2003, "Recent Applications of Viscoelastic Damping for Noise Control in Automobiles and Commercial Airplanes," J. Sound Vib., **262**(3), pp. 457–474.
[35] Collins, T., and Kochersberger, K., 2011, "Constrained Layer Damping Test Results for Aircraft Landing Gear," *Structural Dynamics, Volume 3: Proceedings of the 28th IMAC, a Conference on Structural Dynamics, 2010*, T. Proulx, ed., Springer, New York, pp. 303–314.
[36] Jacobsen, A. J., Barvosa-Carter, W., and Nutt, S., 2007, "Compression Behavior of Micro-Scale Truss Structures Formed From Self-Propagating Polymer Waveguides," Acta Mater., **55**(20), pp. 6724–6733.
[37] ASTM, 2010, "Standard Test Method for Measuring Vibration-Damping Properties of Materials," ASTM International, West Conshohocken, PA, Standarad No. ASTM E756–05.
[38] Macaloney, N., Bujanda, A., Jensen, R., and Goulbourne, N., 2007, "Viscoelastic Characterization of Aliphatic Polyurethane Interlayers," Army Research Laboratory, Aberdeen, MD, Report No. ARL-TR-4296.
[39] Budiansky, B., 1999, "On the Minimum Weights of Compression Structures," Int. J. Solids Struct., **36**(24), pp. 3677–3708.